Active sites of Te-hyperdoped silicon by hard x-ray photoelectron spectroscopy

Moritz Hoesch ✉ ; Olena Fedchenko ; Mao Wang ; Christoph Schlueter ; Dmitrii Potorochin ;
Katerina Medjanik; Sergey Babenkov; Anca S. Ciobanu ; Aimo Winkelmann ; Hans-Joachim Elmers ;
Shengqiang Zhou ; Manfred Helm ; Gerd Schönhense

Check for updates

CrossMark

View Online   Export Citation

28 June 2023 11:37:26

Active sites of Te-hyperdoped silicon by hard x-ray photoelectron spectroscopy

View Online   Export Citation   CrossMark

Moritz Hoesch,[1,a)] Olena Fedchenko,[2] Mao Wang,[3] Christoph Schlueter,[1] Dmitrii Potorochin,[1,4] Katerina Medjanik,[2] Sergey Babenkov,[2] Anca S. Ciobanu,[1] Aimo Winkelmann,[5] Hans-Joachim Elmers,[2] Shengqiang Zhou,[3] Manfred Helm,[3] and Gerd Schönhense[2]

AFFILIATIONS

[1]Deutsches Elektronen-Synchrotron DESY, Notkestr. 85, 22607 Hamburg, Germany
[2]Johannes Gutenberg-Universität, Institut für Physik, 55128 Mainz, Germany
[3]Helmholtz-Zentrum Dresden-Rossendorf, Institute of Ion Beam Physics and Materials Research, Bautzner Landstraße 400, 01328 Dresden, Germany
[4]TU Bergakademie Freiberg, Institute of Experimental Physics, 09599 Freiberg, Germany
[5]Academic Centre for Materials and Nanotechnology (ACMiN), AGH University of Krakow, 30–059 Kraków, Poland

[a)]Author to whom correspondence should be addressed: moritz.hoesch@desy.de

ABSTRACT

Multiple dopant configurations of Te impurities in close vicinity in silicon are investigated using photoelectron spectroscopy, photoelectron diffraction, and Bloch wave calculations. The samples are prepared by ion implantation followed by pulsed laser annealing. The dopant concentration is variable and high above the solubility limit of Te in silicon. The configurations in question are distinguished from isolated Te impurities by a strong chemical core level shift. While Te clusters are found to form only in very small concentrations, multi-Te configurations of type dimer or up to four Te ions surrounding a vacancy are clearly identified. For these configurations, a substitutional site location of Te is found to match the data best in all cases. For isolated Te ions, this matches the expectations. For multi-Te configurations, the results contribute to understanding the exceptional activation of free charge carriers in hyperdoping of chalcogens in silicon.

Doping of the band semiconductor silicon follows well-established principles: To enhance hole (electron) concentration, elements of group 13 (group 15) of the periodic table are introduced leading to singly ionized impurities.[1] Doping to very high limits can lead to a transition to a metallic state above the insulator-to-metal transition (IMT). For these singly ionized dopants, the IMT matches well with the expectations from the band model of Mott.[2] For doubly ionized dopants of group 16, one column further in the periodic table, a similar transition criterion holds, as studied in the case of Si:Se[3] and Si:Te.[4] Above the IMT, the free carrier concentration is in principle freely tunable by the dopant concentration. However, the mutual interaction of dopant atoms may modify their wave functions and their ability to contribute free carriers, which depends also on the local structure surrounding the dopant as well as structural distortions that may occur as two or more of the dopant atoms come in close vicinity.[5,6] For almost all singly ionizing n-type doped silicon studied to date, the formation of donor pairs, clusters, or defect complexes results

in an intrinsic upper limit at around $5 \times 10^{20}\,\mathrm{cm^{-3}}$ for the electron concentration.[6–9]

Surprisingly, hyperdoping of silicon by Te results in electron concentration up to $8.3 \times 10^{20}\,\mathrm{cm^{-3}}$ without saturation.[4,10] It can be assumed that the double-ionized nature of Te in silicon contributes to continued activation also of multi-Te complexes. A part of the charge may be trapped, but in contrast to single-ionized donors part of the charge remains active even in dimers or vacancy configurations. This has been studied theoretically for Se in silicon.[11,12] Chalcogen ions are deep level donors in silicon and have low thermal solubilities.[13] Hyperdoping refers to doping above the solubility limit. It is realized by non-thermal equilibrium methods, e.g., combining ion implantation and pulsed laser melting at nanoseconds.[3,10,14] Potential applications of the hyperdoped silicon include the use as extended photodetectors in the infrared wavelength range.[14–18]

In this Letter, we address the identification of Te sites within the Si matrix. These are observed in samples of Si:Te at high doping

concentration. We combine the method of photoelectron spectroscopy, which is sensitive to the electronic configuration of the dopant atom and its local surrounding, with the analysis of diffraction patterns of these photoelectrons that reveal the geometric configuration of the dopant site. This virtue of the method has also been used in other impurity systems.[19,20] For the same crystal class, at lower photoelectron kinetic energy, studies have been performed on Si:As[21] and diamond:P[22] and summarized in a recent review.[23] We find that the vast majority of Te atoms are located on substitutional sites, which continues to be the case when Te in isolated monomers become the minority against dimer or more complex configurations of nearby Te impurities. For these, model cases are identified, thus rationalizing the ability of complex Te-Si configurations to contribute actively to the conductivity of Si above the IMT.

Samples of Si:Te with peak Te concentrations up to 4.5 at. % have been prepared by ion implantation followed by pulsed laser melting.[10] Te impurities are located in a layer of approximately 100 nm thickness near the surface.[24] The experiments were performed using x-ray photoelectron spectroscopy (XPS) at beamline P22 of the storage ring x-ray source PETRA III[25] at a high photon energy and, thus, photoelectron kinetic energy (around 5690 eV for most data). Due to an inelastic mean free path of approximately 5 nm in this regime,[26] the probing depth can be as high as 20 nm and reaches a region of near peak Te concentration. The top surface of the Si(001) wafers was etched just prior to the experiments using diluted hydrofluoric acid (HF at 10%) followed by a pure ethanol wash and rapid introduction into the vacuum system. The samples were held at the temperature of 40 K during data taking.
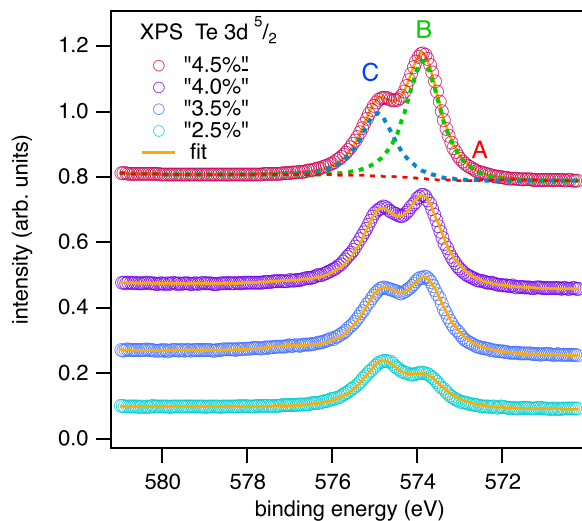

FIG. 1. X-ray photoelectron spectra of samples with varying Te nominal concentration in the Te $3d_{5/2}$ region. The data for nominal concentration of 2.5%, 3.5%, and 4.0% are scaled as acquired with a hemispherical photoemission analyzer, and the increasing Te content is visible through increasing total peak area. The data for "4.5%" (acquired with the time-of-flight spectrometer) are scaled to match. Offsets are introduced for graphical clarity. The best fit spectra are shown as orange lines as described in the text. For "4.5%," the separate contributions from peak C and background, peak B, and peak A are shown as red-, green-, and blue-dashed lines, respectively.

Spectra of x-ray photoelectron spectroscopy (XPS) are shown in Fig. 1 for samples of nominal Te concentration between 2.5 and 4.5 at. %. The peak heights related to Te are found to increase accordingly. A multi-peak structure of at least two chemically shifted peaks is found in all samples in the region of Te $3d_{5/2}$. Chemical shifts in XPS can derive partially from the charge state of the probed ion and from its electrostatic environment. Further and often strong shifts are derived from the dynamical screening of the core hole created in photoemission due to quasi-free and metallic charge carriers. This screening usually results in an observed reduced binding energy. The peak width of each chemically shifted component is ultimately limited by the uncertainty introduced by core hole lifetime, and the final spectrum is composed of the sum of these overlapping contributions. A peak fitting analysis was performed using the CasaXPS software.[27] Details of this analysis and numerical results are shown in the supplementary material. This multi-peak structure is indicative of a variation of impurity ion configurations in the highly doped samples. The peak at lower binding energy (B) grows more rapidly than the peak at 1 eV higher binding energy (C). At the lowest doping concentration, where mostly substitutional site occupation of Te has previously been identified,[10] peak B is significantly smaller than peak C. Intensity C is, thus, related to substitutional Te monomers, i.e., Te ions surrounded by at least one shell of Si in a lattice that is only locally distorted.

We now consider the high-energy photoelectron diffraction (hXPD) patterns generated by emission from these chemically shifted species. The data have been acquired using time-of-flight momentum microscopy[28] for the highest doped sample "4.5%." For photoemission from a Si 2p core level, a pattern of this kind is shown in Fig. 2(d). Note that the photon energy was tuned to excite the electrons from the Si core level to the same $E_{kin} = 5690$ eV as from the Te $3d_{5/2}$ level. The Kikuchi bands of enhanced photoemission intensity as well as characteristic low-intensity trenches are well-described by electron diffraction calculations assuming a point-like emitter.[29] Since each pixel of these patterns is related to a full spectrum, albeit at reduced counting statistics, we can resolve the diffraction patterns for each chemical shift. These are shown in Figs. 2(a)–2(c) for Te 3d. Three distinct patterns are extracted by a pixel-by-pixel decomposition that extracts the intensities of three Gaussian peaks of equal widths and fixed positions.
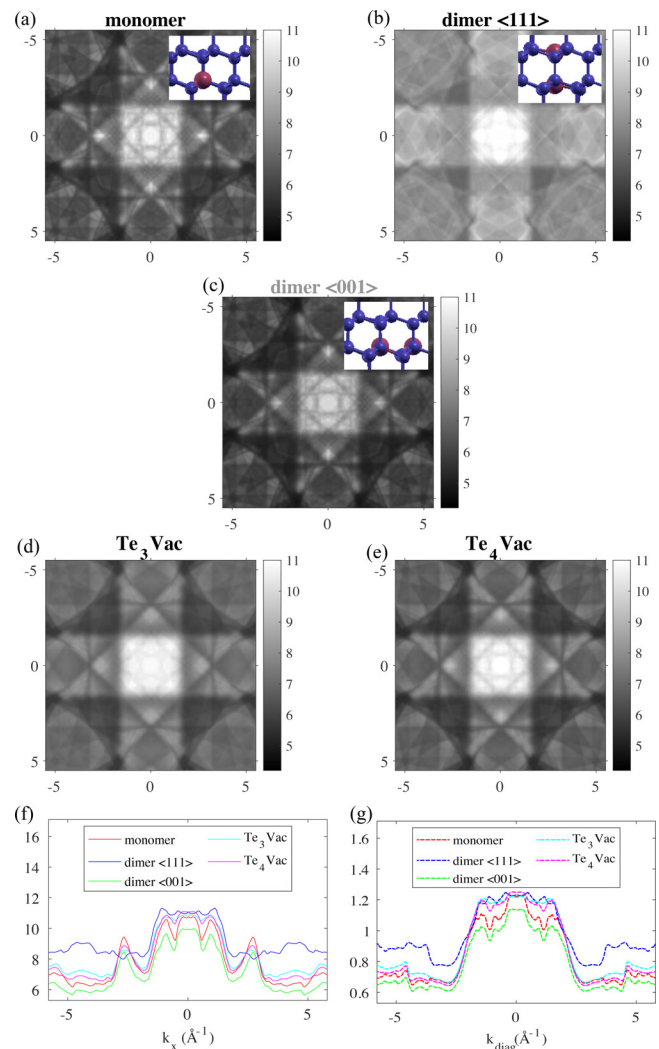
All patterns follow the fourfold symmetry of the Si(001) surface. The patterns have, thus, been symmetrized after checking the fourfold structure. The incidence of the photon beam was along the k_x direction in these plots, or equivalently from $-k_x$ or $\pm k_y$ since the fourfold symmetrization reduces the weak effect of directionality of the photon beam. The incidence angle was 78° from the surface normal, and linearly polarized radiation was used. Pattern A is nearly featureless, but the characteristic trenches parallel to the k_x and k_y axes are also seen in this pattern, at identical positions to the other patterns. Patterns B and C have a striking resemblance to emission from Si. For pattern C, this is expected as this binding energy region belongs to substitutional monomers. Pattern B is of highest intensity, but its overall contrast is further reduced, which will be discussed below. Note that the Kikuchi pattern is sensitive to a displacement of the emitter position with respect to the long range registered lattice site,[29,30] and the monomer is located on the same high symmetry position as a Si atom.

Calculations for the analysis of these patterns proceed in two steps. For electronic structure calculations, we construct supercells of
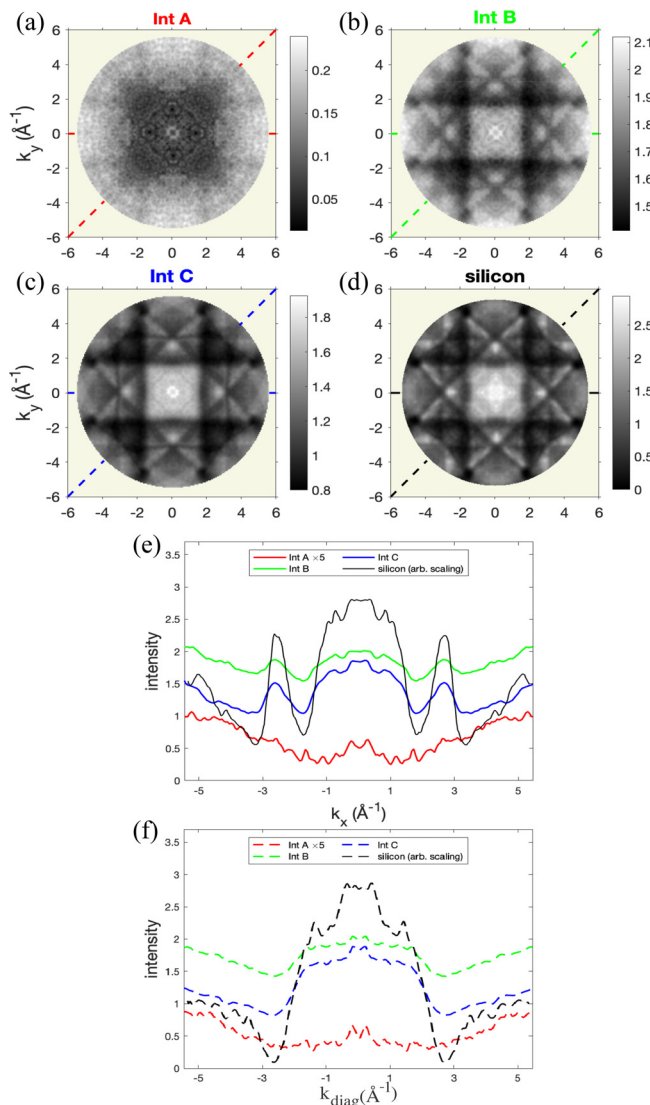
FIG. 2. (a)–(d) hXPD patterns recorded for the sample "4.5%." The patterns Int A–Int C correspond to a decomposition of binding energies as indicated in Fig. 1. The pattern for silicon was recorded for Si 2p at the same kinetic energy as the Te $3d_{5/2}$ level. The line plots in (e) and (f) show cuts through the centers of all patterns, as indicated by colored dashes in (a)–(d).

FIG. 3. (a)–(e) Calculated Bloch wave diffraction patterns for five local structure models as indicated above each panel. Insets in (a)–(c) show the crystal structure viewed along $\langle 110 \rangle$. The line plots shown in (f) and (g) are along the $k_y = 0$ line and the $k_x = k_y$ line, respectively.

$3 \times 3 \times 3$ cubic Si unit cells and introduce one, two, or more Te atoms as well as vacancies. By *ab initio* density functional theory (DFT), we determine the total-energy-minimized configuration for these configurations, thus leading to force free relaxed cells. The DFT model parameters within wien2k[31] are given in the supplementary material. Vacancy-free configurations that we have considered are a substitutional monomer, a substitutional dimer of nearest neighbors $(dim_{\langle 111 \rangle})$, and a configuration of two substitutional Te atoms interspaced by a Si atom $dim_{\langle 100 \rangle}$. Configurations with a vacancy and up to four Te atoms in direct vicinity to the vacancy are labeled Te_nVac with $n = 1 - 4$. In a second step, the hXPD patterns are calculated for the

Te emitter atoms in these configurations by Bloch wave diffraction calculations.[29,32]

The hXPD patterns for five selected configurations are shown in Fig. 3. On inspection we note the similarity of the calculations for the monomer and for the $dim_{\langle 100 \rangle}$, Te_3Vac, and Te_4Vac configurations to each other. All patterns also compare well as to the experimental data of intensities (B) and (C). The $dim_{\langle 111 \rangle}$ and the configurations shown in the supplementary material (Fig. S4) match the data less well.

The diffraction patterns are generally well reproduced by calculations, with the exception of pattern A. We assign this pattern to clusters of Te atoms with the low binding energy arising from Te atoms in clusters. Since pure Te is metallic, photoemission from these clusters will lead to a strong chemical shift to lower binding energies. The clusters may occur in various orientations with respect to the Si lattice and

have a partially amorphous structure, thus leading to the near feature-less pattern. These Te atoms in clusters are a small minority of all Te atoms, given the very small spectral intensity.

A particularly good match is found for the monomer pattern C. Just the total contrast is smaller than that of the calculation, while this contrast is well reproduced in calculations of pure Si.[29] We assign this reduced contrast to differences of vibrational amplitudes between Si matrix atoms and a Te impurity that are not accounted for in our model. Also, any spillover of intensity from the lower binding energy features B and A due to inelastic scattering will reduce the contrast in feature C.

Feature B shows still lower contrast in the experimental data, while the best-matching calculation is $dim_{\langle 100 \rangle}$, Te_3Vac, and Te_4Vac. We have tested further configurations, namely, Te_1Vac and Te_2Vac, but these also led to a rather poor match between cal-culation and pattern B. A reasonable match is found for a tetrago-nal interstitial configuration, since this has the same local symmetry as a substitutional site (see also Ref. 29). This calculation is, however, not physical as it omits the DFT relaxation step. When relaxed, this structure assumes the hexagonal interstitial configura-tion, which has a different symmetry and a very poor match to any of the observed patterns.

We tentatively conclude that pattern B arises from a mixture of configurations $dim_{\langle 001 \rangle}$, Te_3Vac, and Te_4Vac that are present in the sample. Other configurations, namely, $dim_{\langle 111 \rangle}$, are present at signifi-cantly smaller concentrations, at most a small fraction of all contribu-tions to peak B. They may exist as a minority, and their contribution leads to a further reduction of the contrast of pattern B. The configura-tions Te_3Vac and Te_4Vac contain an isolated vacancy, evidence for which has also been found by recent positron annihilation experi-ments in samples of similar preparation.[33] Theoretical support for a significant formation of multi-chalcogen vacancy configurations was found also in the case of Si:Se by first principles simulations, suggesting the likely formation of Te_3Vac and Te_4Vac.[11]

For a quantitative analysis, we assert that peak C (34.5% of total XPS intensity) derives purely from monomers, and peak B (64.8% of XPS intensity) derives from multi-Te configurations. Since each Te atom contributes equally to the photoemission signal, this allows to estimate that about 1/3 of Te in sample "4.5%" is in monomers and 2/3 of Te in multi-Te configurations ($dim_{\langle 111 \rangle}$, $dim_{\langle 001 \rangle}$, Te_2Vac, Te_3Vac, and Te_4Vac). Te in clusters (peak A) is nearly negligible. Further assuming that each multi-Te impurity contains 2.5 ± 0.4 Te ions, the ratio of monomer impurities to multi-Te impurities is 1.38 ± 0.22.

The variation in binding energy can be due to a different charge state of the Te ions, or due to a difference in screening, or a combina-tion of both. For pattern A, we have already identified poorly ionized Te atoms in clusters leading to an electrostatic binding energy reduc-tion. The configurations monomer, $dim_{\langle 111 \rangle}$, $dim_{\langle 001 \rangle}$, Te_3Vac, and Te_4Vac, on the other hand, all correspond to strongly ionized Te. This is evident from the density of states (DOS) extracted from the calcula-tions and shown in Fig. 4. All configurations show a similar Fermi energy ($E - \mu$ of the conduction band minimum CBM) of around 0.3 eV. In addition, a shallow core level of Te at $E_B = 5.1$ eV is found at near identical energy in these calculations (shown in the supplemen-tary material Fig. S6). The electrostatic environment of Te in these five configurations is, thus, similar, and the difference in binding energy
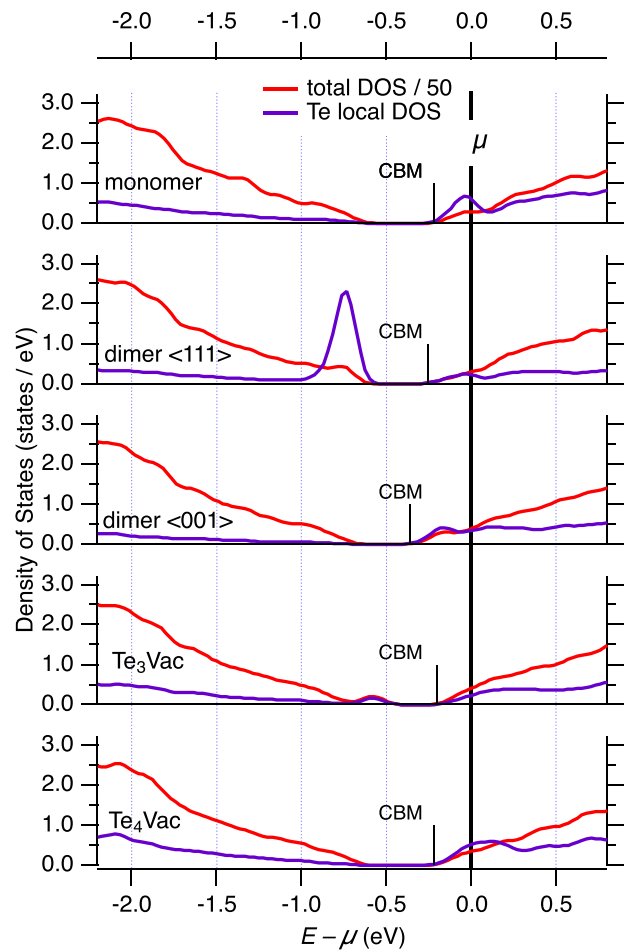
FIG. 4. Density of states and local density of states at the Te site, obtained from *ab initio* calculated supercells with local structures as indicated. The energy is scaled relative to the chemical potential μ. The conduction band minimum (CBM) is indi-cated for each case.

must derive from dynamics in the photoemission process. In $dim_{\langle 111 \rangle}$, $dim_{\langle 001 \rangle}$, Te_3Vac, and Te_4Vac, the close vicinity of doubly ionized Te atoms and the increased local density of free carriers lead to increased screening when compared to the monomer case, which results in a reduced binding energy.

In summary, we have observed a multi-peak structure of the Te core level Te $3d_{5/2}$. A small component (A) of the spectra is identified as arising from Te clusters. The high binding energy component (C) is readily identified as belonging to substitutional monomers. Component (B) also gives a clear and similar photoelectron diffraction pattern. Calculations of selected multi-Te configurations of Te in the silicon matrix are compared to these experimental data. The resulting patterns for $dim_{\langle 111 \rangle}$, Te_1Vac, and Te_2Vac do not match the data well. These multi-Te configurations may still be present in the sample, but as a minority. $Dim_{\langle 100 \rangle}$ as well as Te_3Vac and Te_4Vac with vacancies give a good match to the experimental data. Therefore, the data strongly support a large fraction of Te in such configurations and only a minority in regular dimers or other configurations.

Inspection of the model calculations in regard to the density of states shows that ionization of Te is similar in all configurations, thus demonstrating the double-donor quality of Te also in the complex configurations. The high local density of free charge carriers is also held responsible for the chemical shift of the core level to lower binding energy. This strong ability of Te to supply electrons in both monomer and multi-Te configurations serves to explain the previously observed saturation-free increase in metallic carrier density in Te-hyperdoped silicon.

See the supplementary material for XPS spectra over a larger binding energy range (Fig. S1), as well as from additional sample preparations (Fig. S2), which details their fitting procedure and summarizes the numerical results (Table S1); an alternative, simpler data reduction method is introduced and the corresponding results are shown (Fig. S3); modeling calculation results from cases incompatible with the experimental data are presented (Fig. S4); the DOS for these cases is shown along with the DOS for pure silicon (Fig. S5); the findings of DOS for all model cases over a high binding energy range are summarized (Fig. S6); and all numerical results of the XPS fitting procedure are given in a table figure.

AUTHOR DECLARATIONS

Conflict of Interest

The authors have no conflicts to disclose.

Author Contributions

Moritz Hoesch: Conceptualization (lead); Data curation (equal); Formal analysis (supporting); Investigation (lead); Supervision (equal); Visualization (lead); Writing – original draft (lead). **Hans-Joachim Elmers:** Investigation (equal); Resources (equal); Supervision (equal); Writing – review & editing (equal). **Shengqiang Zhou:** Resources (lead); Writing – review & editing (equal). **Manfred Helm:** Resources (equal); Supervision (equal); Writing – review & editing (equal). **Gerd Schönhense:** Conceptualization (equal); Investigation (equal); Methodology (equal); Resources (equal); Supervision (equal); Writing – review & editing (equal). **Olena Fedchenko:** Data curation (equal); Formal analysis (equal); Investigation (equal). **Mao Wang:** Investigation (equal); Resources (equal); Writing – review & editing (equal). **Christoph Schlueter:** Data curation (equal); Investigation (equal); Methodology (equal); Resources (equal); Writing – review & editing (equal). **Dmitrii Potorochin:** Data curation (equal); Formal analysis (equal); Writing – review & editing (equal). **K. Medjanik:** Resources (equal); Writing – review & editing (equal). **Sergey Babenkov:** Resources (equal); Writing – review & editing (equal). **Anca Simona Ciobanu:** Methodology (equal); Resources (equal); Writing – review & editing (equal). **Aimo Winkelmann:** Data curation (equal); Formal analysis (lead); Supervision (equal); Writing – review & editing (equal).

DATA AVAILABILITY

The data that support the findings of this study are available from the corresponding author upon reasonable request.

REFERENCES

[1] G. L. Pearson and J. Bardeen, Phys. Rev. **75**, 865 (1949).
[2] N. F. Mott, *Metal-Insulator Transitions* (Taylor and Francis, London, 1974).
[3] E. Ertekin, M. T. Winkler, D. Recht, A. J. Said, M. J. Aziz, T. Buonassisi, and J. C. Grossman, Phys. Rev. Lett. **108**, 026401 (2012).
[4] M. Wang, A. Debernardi, W. Zhang, C. Xu, Y. Yuan, Y. Xie, Y. Berencén, S. Prucnal, M. Helm, and S. Zhou, Phys. Rev. B **102**, 085204 (2020).
[5] P. Voyles, D. Muller, J. Grazul, P. Citrin, and H.-J. Gossmann, Nature **416**, 826 (2002).
[6] M. Rummukainen, I. Makkonen, V. Ranki, M. J. Puska, K. Saarinen, and H.-J. L. Gossmann, Phys. Rev. Lett. **94**, 165501 (2005).
[7] D. J. Chadi, P. H. Citrin, C. H. Park, D. L. Adler, M. A. Marcus, and H.-J. Gossmann, Phys. Rev. Lett. **79**, 4834 (1997).
[8] V. Ranki, J. Nissilä, and K. Saarinen, Phys. Rev. Lett. **88**, 105506 (2002).
[9] R. Pinacho, M. Jaraiz, P. Castrillo, I. Martin-Bragado, J. E. Rubio, and J. Barbolla, Appl. Phys. Lett. **86**, 252103 (2005).
[10] M. Wang, A. Debernardi, Y. Berencén, R. Heller, C. Xu, Y. Yuan, Y. Xie, R. Böttger, L. Rebohle, W. Skorupa, M. Helm, S. Prucnal, and S. Zhou, Phys. Rev. Appl. **11**, 054039 (2019).
[11] A. Debernardi, Phys. Chem. Chem. Phys. **23**, 24699 (2021).
[12] A. Debernardi, Semicond. Sci. Technol. **38**, 014002 (2023).
[13] K. Sánchez, I. Aguilera, P. Palacios, and P. Wahnón, Phys. Rev. B **82**, 165201 (2010).
[14] J. M. Warrender, Appl. Phys. Rev. **3**, 031104 (2016).
[15] A. J. Said, D. Recht, J. T. Sullivan, J. M. Warrender, T. Buonassisi, P. D. Persans, and M. J. Aziz, Appl. Phys. Lett. **99**, 073503 (2011).
[16] X. Jin, Y. Sun, Q. Wu, Z. Jia, S. Huang, J. Yao, H. Huang, and J. Xu, ACS Appl. Mater. Interfaces **11**, 42385 (2019).
[17] M. Wang, E. García-Hemme, Y. Berencen, R. Hübner, Y. Xie, L. Rebohle, C. Xu, H. Schneider, M. Helm, and S. Zhou, Adv. Opt. Mater. **9**, 2001546 (2021).
[18] E. Rosseel, M. Tirrito, C. Porret, B. Douhard, J. Meersschaut, A. Y. Hikavyy, R. Loo, N. Horiguchi, G. Pourtois, and N. Nakazaki, ECS Trans. **93**, 11 (2019).
[19] K. Medjanik, O. Fedchenko, O. Yastrubchak, J. Sadowski, M. Sawicki, L. Gluba, D. Vasilyev, S. Babenkov, S. Chernov, A. Winkelmann, H. J. Elmers, and G. Schönhense, Phys. Rev. B **103**, 075107 (2021).
[20] O. Fedchenko, A. Winkelmann, and G. Schönhense, J. Phys. Soc. Jpn. **91**, 091006 (2022).
[21] K. Tsutsui, T. Matsushita, K. Natori, T. Muro, Y. Morikawa, T. Hoshii, K. Kakushima, H. Wakabayashi, K. Hayashi, F. Matsui, and T. Kinoshita, Nano Lett. **17**, 7533 (2017).
[22] T. Yokoya, K. Terashima, A. Takeda, T. Fukura, H. Fujiwara, T. Muro, T. Kinoshita, H. Kato, S. Yamasaki, T. Oguchi, T. Wakita, Y. Muraoka, and T. Matsushita, Nano Lett. **19**, 5915 (2019).
[23] T. Yokoya, J. Phys. Soc. Jpn. **91**, 091007 (2022).
[24] M. Wang, Y. Berencén, E. García-Hemme, S. Prucnal, R. Hübner, Y. Yuan, C. Xu, L. Rebohle, R. Böttger, R. Heller, H. Schneider, W. Skorupa, M. Helm, and S. Zhou, Phys. Rev. Appl. **10**, 024054 (2018).
[25] C. Schlueter, A. Gloskovskii, K. Ederer, I. Schostak, S. Piec, I. Sarkar, Y. Matveyev, P. Lömker, M. Sing, R. Claessen, C. Wiemann, C. M. Schneider, K. Medjanik, G. Schönhense, P. Amann, A. Nilsson, and W. Drube, AIP Conf. Proc. **2054**, 040010 (2019).
[26] M. P. Seah and W. A. Dench, Surf. Interface Anal. **1**, 2 (1979).

28 June 2023 11:37:26

[27]N. Fairley, V. Fernandez, M. Richard-Plouet, C. Guillot-Deudon, J. Walton, E. Smith, D. Flahaut, M. Greiner, M. Biesinger, S. Tougaard, D. Morgan, and J. Baltrusaitis, Appl. Surf. Sci. Adv. **5**, 100112 (2021).

[28]K. Medjanik, S. V. Babenkov, S. Chernov, D. Vasilyev, B. Schönhense, C. Schlueter, A. Gloskovskii, Y. Matveyev, W. Drube, H. J. Elmers, and G. Schönhense, J. Synchrotron Radiat. **26**, 1996 (2019).

[29]O. Fedchenko, A. Winkelmann, S. Chernov, K. Medjanik, S. Babenkov, S. Y. Agustsson, D. Vasilyev, M. Hoesch, H.-J. Elmers, and G. Schönhense, New J. Phys. **22**, 103002 (2020).

[30]A. Winkelmann and M. Vos, Ultramicroscopy **125**, 66 (2013).

[31]P. Blaha, K. Schwarz, G. Madsen, D. Kvasnicka, and J. Luitz, *Wien2k: An Augmented Plane Wave Plus Local Orbitals Program for Calculating Crystal Properties* (Techn. Universität, Austria, 2001).

[32]A. Winkelmann, C. S. Fadley, and F. J. G. de Abajo, New J. Phys. **10**, 113002 (2008).

[33]M. Shaikh, M. Wang, R. Hübner, M. Liedke, M. Butterling, D. Solonenko, T. Madeira, Z. Li, Y. Xie, E. Hirschmann, A. Wagner, D. Zahn, M. Helm, and S. Zhou, Appl. Surf. Sci. **567**, 150755 (2021).

28 June 2023 11:37:26